Research Square

Preprints are preliminary reports that have not undergone peer review.
They should not be considered conclusive, used to inform clinical practice,
or referenced by the media as validated information.

Two- and three-dimensional electrical resistivity tomography of a sinkhole-affected residential area on reclaimed coastal land, Cua Ong, Quang Ninh City, northern Vietnam

Trung Nhu Nguyen

nntrung@ies.vast.vn

Vietnam Academy of Science and Technology https://orcid.org/0000-0002-6942-8502

Duong Van Nguyen

Vietnam Academy of Science and Technology

Truyen The Pham

Vietnam Academy of Science and Technology

Nam Van Bui

Vietnam Academy of Science and Technology

Kha Van Tran

Vietnam Academy of Science and Technology

Diep Van Nguyen

Vietnam Academy of Science and Technology

Giang Thi Ha

Vietnam Academy of Science and Technology

Research Article

Keywords: Electrical resistivity tomography, 3-D inversion, Sinkhole, Land reclamation, Covered karst, Saline groundwater

Posted Date: November 12th, 2026

DOI: https://doi.org/10.21203/rs.3.rs-11462429/v1

License: This work is licensed under a Creative Commons Attribution 4.0 International License.
Read Full License

Two- and three-dimensional electrical resistivity tomography of a sinkhole-affected residential area on reclaimed coastal land, Cua Ong, Quang Ninh City, northern Vietnam

Nguyen Nhu Trung[1,*], Nguyen Van Duong[1], Pham The Truyen[1], Bui Van Nam[1], Tran Van Kha[1], Nguyen Van Diep[1], Ha Thi Giang[1,2]

[1]Institute of Earth Sciences, Vietnam Academy of Science and Technology, Hanoi, Vietnam

[2]University of Mining and Geology

*Corresponding author: nntrung@ies.vast.vn · ORCID: 0000-0002-6942-8502

Abstract

Sinkholes recur in the Thuy Son residential area of Cua Ong, Quang Ninh City, northern Vietnam, built on reclaimed coastal land. Twelve electrical resistivity tomography (ERT) lines (3951 data) were inverted in 2-D and jointly in 3-D. At six line crossings the two 2-D models differ by a median factor of 2.7; the 3-D model is consistent by construction and departs from them by a median factor of 1.8. The 2-D sections resolve layer boundaries beneath each line, whereas only the 3-D model maps units between lines. A strongly conductive layer (mostly below 3 Ωm) underlies the centre and west of the grid and reaches 20–50 m depth; more resistive ground occurs in the north-east and beneath part of the south-east. Three existing boreholes in the north-east reached carbonate rock at 7.6–9.0 m depth, and two boreholes there met clay-filled cavities. All 14 recorded sinkholes in the grid lie on 17–64 Ωm ground at 8.7–21.9 m depth, and neither they nor a sinkhole active during the survey lie on the conductive layer. We interpret the conductive layer as thick saline cover over a deepening bedrock surface, and the north-eastern ground as carbonate under thin

cover, so sinkholes occur where thin cover rests on carbonate. This is consistent with suffosion of the cover into karst driven by groundwater movement, which remains to be tested. The sinkhole association rests on one sinkhole-bearing area.

Keywords: Electrical resistivity tomography; 3-D inversion; Sinkhole; Land reclamation; Covered karst; Saline groundwater

1. Introduction

Coastal land reclamation has expanded rapidly along the Ha Long–Cua Ong coast of Quang Ninh City since the 1990s, driven by urban growth and coal mining (Nguyen et al. 2022). Ground built on reclaimed and made land is prone to long-term settlement, chiefly from consolidation of the soft marine clay beneath the fill (Mesri and Funk 2015). Collapses can also occur within the fill itself. Sinkholes in made ground are commonly attributed to internal erosion (suffosion) of fine particles towards defects in buried pipes and drains. Laboratory and numerical studies show that cyclic inflow and drainage at a defect, the hydraulic gradient and the density of the soil control how fast a cavity grows and when its roof fails (Mukunoki et al. 2012; Karoui et al. 2018; Zhang et al. 2020). In Naples, the frequency of anthropogenic sinkholes correlates with rainfall, and damaged service lines are a predisposing factor (Tufano et al. 2022).

Where reclaimed land overlies soluble bedrock, cover material can also be washed down into voids in the rock, and changes in groundwater conditions commonly trigger such sinkholes (Gutiérrez et al. 2014). Along the Cua Ong (former Cam Pha) coast of Quang Ninh City, sinkholes have been recorded since 1998, and boreholes drilled into some of them reached carbonate rock (Tran et al. 2016). Subsidence in the Quang Ninh coal basin has otherwise been studied mainly as an effect of underground mining (Dang et al. 2021).

Electrical resistivity tomography (ERT) is widely used in sinkhole investigations (Zhou et al. 2002; Carbonel et al. 2015; Loke et al. 2013). In urban areas, lines are constrained by buildings and streets, and abrupt resistivity changes across collapse structures can limit what ERT resolves (Sevil et al. 2017). Parallel lines over piping cavities have been combined to map the cavity network in plan (Carrazza et al. 2016). Full 3-D inversion of data from networks of 2-D lines generally gives better models than assembling independent 2-D sections (Chambers et al. 2002; Papadopoulos et al. 2007), and has been applied at a former waste-disposal site (Chambers et al. 2006). Papadopoulos et al. (2007) recommend that line separation not exceed the electrode spacing, a condition rarely met in urban surveys. In coastal settings, very low formation resistivity (about 1–5 Ωm) is commonly attributed to saline pore water (de Franco et al. 2009; Nguyen et al. 2009; Cong-Thi et al. 2021; Nguyen et al. 2025a, 2025b).

This paper reports an ERT survey of a sinkhole-affected reclaimed area at Cua Ong, where twelve lines laid along streets form an irregular network with line separations of 5–105 m. Such networks are common in urban investigations, but how far independent 2-D sections from them agree with one another, and what a joint 3-D inversion adds, have to be assessed in each case. We (1) describe the resistivity structure from twelve 2-D lines; (2) build a 3-D model by joint inversion of all lines, test it against the 2-D models at line crossings and against existing boreholes, and define what each type of analysis can and cannot show; and (3) compare the resistivity structure with the positions of recorded sinkholes and interpret the comparison in terms of groundwater movement.

2. Study area

The survey area is the Thuy Son residential area in the Cua Ong ward, Quang Ninh City. The survey grid is centred at 21.0013° N, 107.3231° E (WGS84; UTM zone 48N 741486 E,

2324045 N) and spans 20.9992–21.0034° N and 107.3212–107.3250° E (Fig. 1a, b). The ground is flat, with spot heights of 3.1–3.4 m (Tran et al. 2016), and the grid covers about 350 m × 420 m (Fig. 1c). It is bounded to the east by the Hoa Chat stream, a channel that carries drainage water from the Deo Nai and Coc Sau open-pit coal mines to the sea; around the time of the 2014 sinkholes its bed was repeatedly dammed into settling ponds to recover coal (Tran et al. 2016). The channel is tidal: seawater flows in on the rising tide and water drains seaward on the falling tide. The area lay seaward of the shoreline mapped before 1966 (Tran et al. 2016) and has since been reclaimed: filling began in 2001, with waste rock from the coal mines of the region, according to local-authority records. Boreholes in the north-east of the grid (Section 3.5) show fill 2.5–4.4 m thick over sand and gravel and gravelly sandy clays, and carbonate rock of the Carboniferous–Permian Bac Son Formation from 7.6–9.0 m depth; the water table in the fill is 0.5–2 m deep (Tran et al. 2016). The coal mines to the north lie within Triassic clastic rocks of the Hon Gai Formation (Tran et al. 2016).

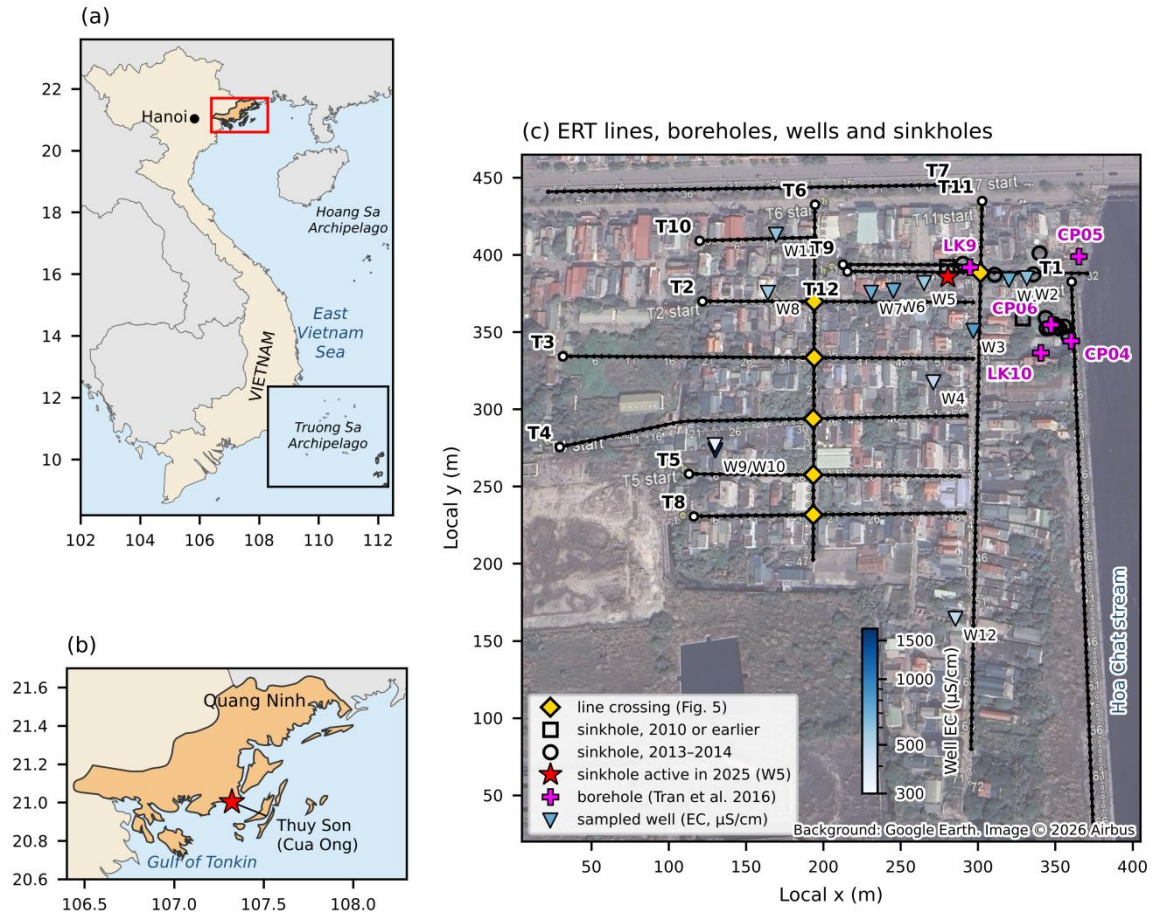


Fig. 1 (a) Location of the study area in Vietnam, with the Hoang Sa Archipelago and, in the inset, the Truong Sa Archipelago; the red box marks panel (b). (b) Quang Ninh City (shaded) and the Thuy Son survey area in Cua Ong ward (star). Base maps from Natural Earth (public domain). (c) Layout of the twelve ERT lines in the local grid (UTM zone 48N rotated by 4.5°) on a Google Earth background (image © 2026 Airbus), lightened for clarity. Dots: electrodes every 5 m; open circle: start of each line (x = 0 m). Yellow diamonds: line crossings compared in Fig. 5. Triangles: sampled wells W1–W12, coloured by EC (Table 3). Red star: sinkhole that appeared during the survey (house of well W5). Squares and circles: recorded sinkholes of 2010 and of 2013–2014, respectively, mapped by Tran et al. (2016). Magenta crosses: boreholes of Tran et al. (2016)

Tran et al. (2016) compiled a sinkhole inventory for the former Cam Pha city, now including Cua Ong, and mapped the sinkholes at Thuy Son at 1:500. Fourteen of them lie inside the survey grid (Fig. 1c): two of 2010, five of 2013 and seven of 2014, about 1–15 m across; they

were later backfilled (Tran et al. 2016). During the ERT survey in October 2025, a new sinkhole appeared at the house of well W5 (Section 4.5).

3. Data and methods

3.1 Data acquisition

Twelve ERT lines (T1–T12) were measured in October 2025 with a 72-electrode Syscal Pro system (IRIS Instruments) using the Wenner–Schlumberger array with 5 m electrode spacing (Table 1; Fig. 1c). Line lengths are 75–355 m (2575 m in total). Most lines run approximately east–west; T1, T6 and T11 run approximately north–south and cross the others. Most electrodes were placed on concrete pavement, in holes drilled through the concrete before the stakes were driven. Contact resistances recorded by the instrument had line medians of 0.3–1.8 kΩ, and injected currents had line medians of about 410–790 mA. The stacking deviation recorded for each measurement had line medians of 0.04–0.9%; it was highest on the most conductive lines (T3–T5 and T8), where the measured potentials were smallest (line medians of about 2–3 mV). Data with large misfits were removed with the error-statistics tool of Res2DInv, which displays the distribution of the misfit between measured and calculated apparent resistivities after a trial inversion so that data with large misfits can be deleted before the edited set is inverted again (Seequent 2025). The cut-off was chosen for each line by inspection of the misfit distribution. This left 3951 of the 6140 recorded measurements (Table 1). Electrode positions were computed along the surveyed line traces at the nominal 5 m spacing, from x = 0 m at electrode 1, between line ends positioned with a handheld GPS receiver, so that positions are accurate to a few metres. The ground surface is nearly flat (spot heights of 3.1–3.4 m; Section 2), and all inversions assumed flat topography.

Table 1 ERT lines and inversion statistics. RMS: final root-mean-square misfit of the 2-D inversion. r: correlation coefficient between $\log_{10}$ resistivity of the 2-D model cells and of the 3-D model sampled at the same positions

Line	Length (m)	Electrodes	Data	2-D iterations	2-D RMS (%)	r (log ρ, 2-D vs 3-D)
T1	355	72	1088	13	4.0	0.75
T2	175	36	238	25	5.3	0.80
T3	265	54	514	18	4.9	0.91
T4	265	54	373	25	6.5	0.80
T5	175	36	107	25	6.6	0.83
T6	230	47	159	13	6.8	0.76
T7	265	54	204	15	7.8	0.86
T8	175	36	131	11	7.2	0.80
T9	85	18	57	15	4.5	0.92
T10	75	16	26	25	7.7	0.70
T11	355	72	816	13	4.8	0.88
T12	155	32	238	4	4.9	0.86
Total	2575	527	3951			

3.2 Two-dimensional inversion

Each line was inverted with Res2DInv version 4.10.20, which implements the smoothness-constrained least-squares method of Loke and Barker (1996). The same regularisation was used for all lines: L2-norm (smooth) constraints on both data misfit and model roughness, initial and minimum damping factors of 0.15 and 0.02, damping increasing by a factor of 1.05 per layer, a vertical-to-horizontal roughness filter ratio of 1, and model cells 2.5 m wide (half the electrode spacing). Each inversion was continued until the RMS misfit no longer decreased appreciably, so the number of iterations differs between lines (4–25), and the final RMS misfits are 4.0–7.8% (Table 1). These misfits are much larger than the stacking deviations recorded by the instrument (Section 3.1), which measure only random noise within each measurement and not systematic errors such as electrode-position errors or 3-D effects.

3.3 Three-dimensional inversion

All twelve data sets were merged into one file in the general-array, arbitrary point-electrode format of Res3DInv (Seequent 2022). Coordinates were transformed from UTM zone 48N to a local Cartesian frame rotated by 4.5° so that most lines are parallel to the grid axes. The

3951 data use 525 distinct electrode positions (two positions are shared by crossing lines). The model grid has 5 m × 5 m cells over 355 m × 425 m (71 × 85 cells) and ten layers whose thickness increases by a factor of 1.15 from 2.5 m at the surface, giving a base at 50.8 m (60,350 cells in total). Res3DInv version 3.19.0 was used. Robust (L1-norm) constraints were applied to both data misfit and model roughness (Loke et al. 2003; see Chambers et al. 2006 for their use in 3-D). Initial and minimum damping factors were 0.10 and 0.01, and the reference-model damping factor was 0.07.

Four runs were made (Table 2). Run 1 used all data, the finite-difference solver and electrodes assigned to the nearest grid nodes. Runs 2–4 used the finite-element solver on a grid distorted so that nodes coincide with the electrode positions. Run 2 increased the damping of the first layer by a factor of five to suppress near-surface artefacts, but this slowed convergence markedly (misfit 10.7% after five iterations). Run 3 used a first-layer damping factor of two. Each run comprised five iterations.

Before run 4, 50 data (1.3%) were removed. They comprise all 11 data from line T6 that use the electrode at x = 135 m (electrode 28), where T6 crosses T4, and 39 further data whose run-3 misfit exceeded $|\ln(\rho_{a,obs}/\rho_{a,calc})| = 0.5$ (a factor of about 1.65). The T6 data were removed because they showed a systematic misfit in the 3-D inversion: whenever x = 135 m was a potential electrode, the observed apparent resistivity was about 2.0–2.5 times the calculated value, although the same data are fitted to within about 10% by the 2-D inversion of T6 alone. When the electrodes were removed, water spurted from the hole of this electrode: it had been driven into a buried water-filled PVC pipe, which had to be repaired. The pipe and the leaking water probably gave this electrode an anomalous contact with the ground. The 2-D inversion of T6 alone can absorb such an effect in near-surface cells, whereas in 3-D the same ground is also constrained by T4. More generally, T6 probably runs over buried water pipes, and of the lines that cross others it kept the smallest share of its

recorded data (30%). We therefore regard T6 as the least reliable of the crossing lines. Run 4, with the remaining 3901 data, is the preferred model.

Table 2 Res3DInv runs. Misfit is the mean absolute relative misfit reported by the program. LS RMS: least-squares RMS misfit of the last iteration

Run	Data	Forward solver, electrodes	First-layer damping	Misfit after 5 iterations (%)
1	3951	Finite difference, nearest nodes	×1	5.87
2	3951	Finite element, distorted grid	×5	10.67 (LS RMS 19.39)
3	3951	Finite element, distorted grid	×2	7.11
4 (preferred)	3901	Finite element, distorted grid	×2	6.35 (LS RMS 9.83)

Because a formal resolution analysis is computationally impractical for a model of this size, we blanked model cells by a simple geometric criterion: a cell is retained if the horizontal distance from its centre to the nearest electrode does not exceed 10 m plus the depth of the cell centre. This criterion is a pragmatic proxy for sensitivity, not a formal depth-of-investigation analysis (Oldenburg and Li 1999, Deceuster et al. 2014). The retained fraction of the grid increases with depth, from 34% in the top layer to 77% in the deepest layer, because the footprint of each line widens with depth.

The 2-D and 3-D models were compared in two ways. First, the 3-D model was sampled along each line and compared cell by cell with the 2-D section (Fig. 2; Fig. A1; Table 1). Second, at the six points where two lines cross within 3 m of each other, the resistivity–depth profiles of the two 2-D models and of the 3-D model were compared at 1 m depth intervals down to the shallower of the two 2-D models. The difference between two profiles is expressed as a factor, 10 raised to the median absolute difference in $\log_{10} \rho$. Model stability was assessed from the median absolute relative difference between 3-D runs, computed layer by layer over the retained cells.

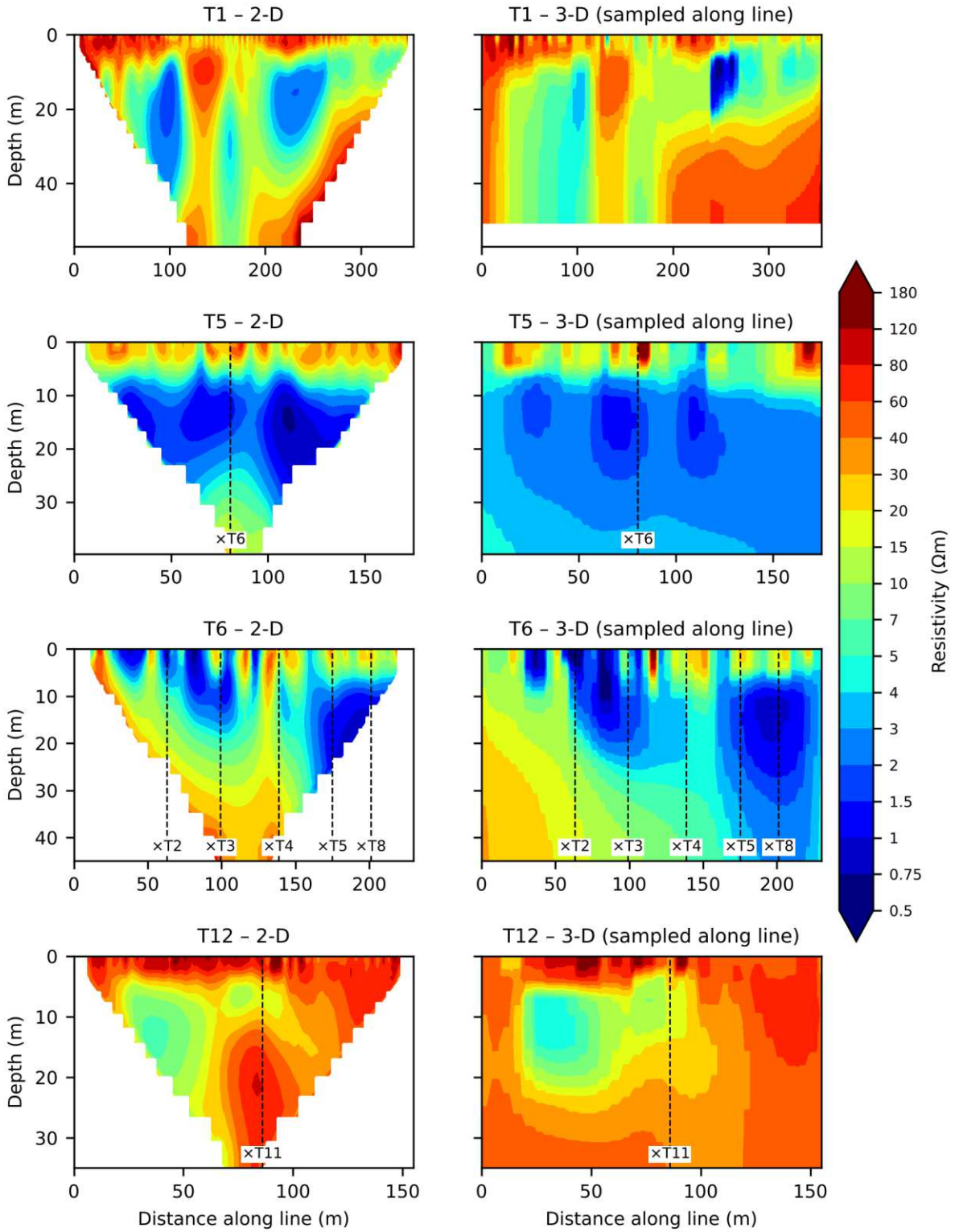


Fig. 2 Resistivity sections along lines T1, T5, T6 and T12 from 2-D inversion (left) and from the 3-D model sampled along the same lines (right), interpolated from the model cells and shown with the same discrete colour scale as Figs. 3 and 7. Dashed lines: positions where other lines cross. All twelve lines are shown in Fig. A1

3.4 Well-water measurements

During the ERT survey, water was sampled from 12 hand-dug domestic wells within the survey grid (Fig. 1c). Most are 2.5–3.5 m deep; W9 is 5 m deep, with the water level at about 3.5 m (static level). Samples were taken from the household pumps, except at W9, which was sampled with a bucket. Electrical conductivity (EC), total dissolved solids (TDS), pH and temperature were measured in the field with a COM600 multi-parameter meter (Total Meter, Taiwan). The meter reported TDS as about 0.5 × EC, so TDS is not an independent measurement. EC was not temperature-compensated in the field; we compensated it to 25 °C (EC_{25}) with a linear coefficient of 0.0187 per °C, the mean value found by Hayashi (2004). For comparison with the ERT, which measures the ground at its in-situ temperature, we used the field EC and computed the pore-water resistivity as $\rho_w = 10^4/EC$ (Ωm, with EC in µS/cm). Well positions were recorded with a handheld GPS receiver and reported to one arc-second (about 30 m). Residents reported that several wells were brackish or saline when dug and became fresh later: W9 after 3–4 years, and W12, dug in 2007, gradually. A new sinkhole, 6–8 m across, appeared at the house of W5 during the survey. For clean, saturated material, Archie's law requires the formation factor ρ/ρ_w to be at least 1 (Archie 1942), so a formation resistivity lower than ρ_w means that the water at that depth is more saline than the sampled water, or that clay adds surface conduction (Waxman and Smits 1968).

3.5 Borehole data

Five boreholes from earlier work lie in the north-east of the grid (Fig. 1c). LK9 and LK10 (labelled LK9-DVL and LK10) belong to the 2013 investigation of the Geophysical Technology Joint Stock Company, compiled by Tran et al. (2016); LK10 was drilled into the sinkhole of 21 August 2013. CP04, CP05 and CP06 were drilled by Tran et al. (2016) from 29 July 2014, the day several sinkholes formed: CP04 and CP06 into new sinkholes and CP05 at a site without subsidence. Logs of LK9, CP04 and CP06 were read from the

engineering-geological section of Tran et al. (2016) to about 0.2 m; for LK10 and CP05 only written descriptions are available (Tran et al. 2016). Positions were read from the graticule of their 1:500 map, on which the sinkholes fall within about 5 m of the inventory positions.

4. Results

4.1 Two-dimensional sections

Most sections show three layers, which we separate at 10 Ωm, ignoring the top 2.5 m (ranges below are 10th–90th percentiles over the cells of each layer on all lines). The upper layer (L1) is resistive (mostly 12–93 Ωm, median 32 Ωm) and extends to the top of L2, typically at 2.6–12 m depth (median 5.8 m). The intermediate layer (L2) is strongly conductive, mostly 1.4–8 Ωm (median 3.7 Ωm), and is most conductive on T4, T5 and T8 (medians 2.1–2.9 Ωm). Where its base is reached, it is typically 6–37 m thick (median 21 m). The lower layer (L3) is mostly 11–40 Ωm (median 17 Ωm), and its base is not reached. Towards the north-east corner of the grid, near the sinkholes, L2 thins or is replaced by material of 10–100 Ωm: on most of T12, on T9, on parts of the eastern half of T2, on the first 105 m of T7 and at the northern ends of T1 and T11. Taking the depth at which resistivity rises back above 10 Ωm beneath L2 as its base (Fig. A2), the median depth to the base is about 20 m on T6, 27 m on T7, 31–35 m on T1, T3, T5 and T8 and 45 m on T4, with values of up to about 51 m; on many profiles the base lies below the 2-D model. Along T11 beyond x ≈ 225 m (y ≈ 100–210 m in the local grid) no layer below 10 Ωm is present: resistivity is 35–120 Ωm from the surface to the base of the section (27–51 m). On T1, about 70 m farther east, L2 is present (2–4 Ωm at 8–27 m), and its base rises southwards from about 35–40 m to 14–17 m.

4.2 Three-dimensional model

The shallow layers of the 3-D model (0–5.4 m) are dominated by short-wavelength variation along the lines (Fig. 3). This probably reflects heterogeneous fill and the lack of data between

lines. From about 5.4 m downwards, a coherent conductive body (mostly below 3 Ωm) occupies the centre and west of the grid, beneath lines T3–T5, T8 and the southern half of T6 (Figs. 3 and 4; Fig. A3). It persists to the base of the covered volume. More resistive material (above about 15 Ωm, locally above 30 Ωm) occurs in three areas: in the north-east corner, around T12, T7 and the northern end of T11, at all depths; beneath T11 south of y ≈ 225 m and, below about 20 m, the southern part of T1, where it extends nearly to the surface on T11; and locally at the western ends of T3 and T4. Between these areas, the central parts of T11 and T1 are moderately conductive (about 3–15 Ωm). Beneath T1 there are also low-resistivity zones at x ≈ 80–110 m (3–5 Ωm) and x ≈ 240–260 m (below 1 Ωm in the upper 12 m), which we do not interpret further.

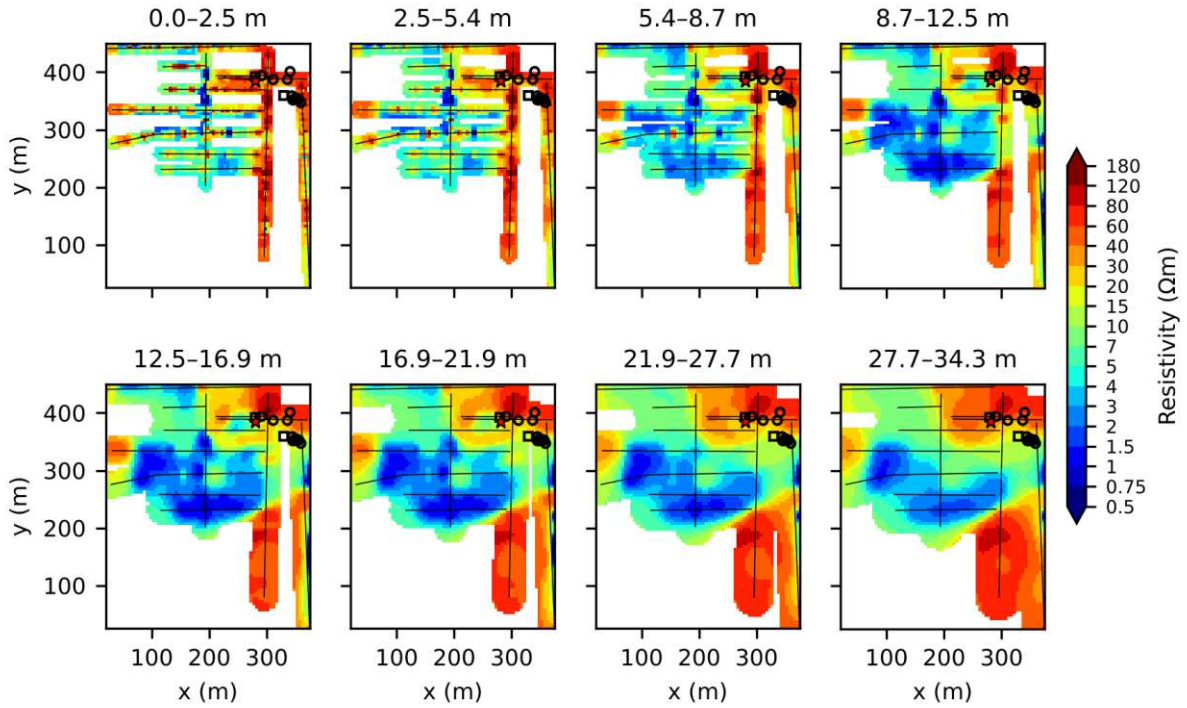


Fig. 3 Depth slices through the preferred 3-D model (run 4) for layers 1–8. Cells farther than 10 m plus their depth from the nearest electrode are blanked. Lines: ERT lines; open symbols: recorded sinkholes

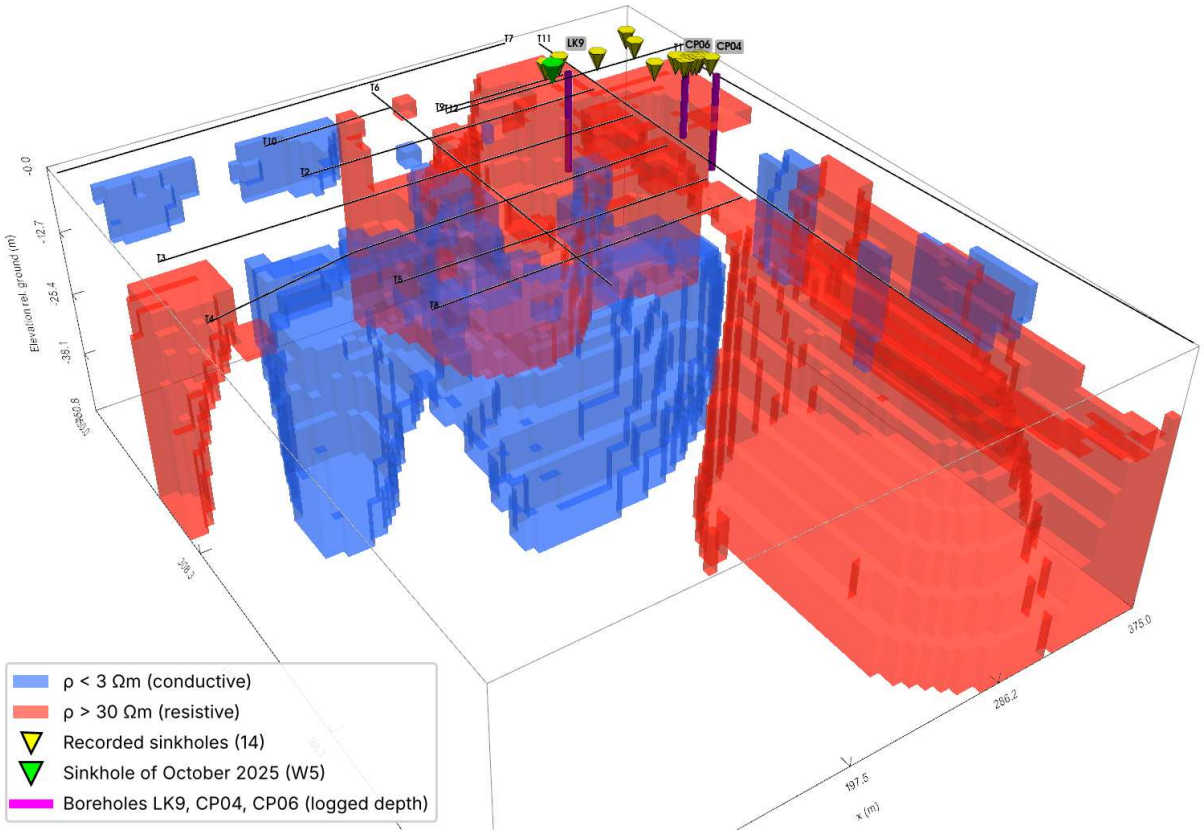


Fig. 4 Perspective view of the preferred 3-D model below 5.4 m depth: volumes with resistivity below 3 Ωm (blue) and above 30 Ωm (red), restricted to covered cells. Vertical exaggeration ×3; the vertical axis is labelled with elevation relative to the ground surface at true scale; rho: resistivity. Yellow cones: the 14 recorded sinkholes inside the grid; green cone: the sinkhole of October 2025 at W5; magenta columns: boreholes LK9, CP04 and CP06 to their logged depth (Tran et al. 2016)

Sampled along the lines, the 3-D model reproduces the main features of the 2-D sections (Fig. 2; Fig. A1). The correlation of log-resistivity between the two is 0.70–0.92 per line (Table 1), and the RMS difference in $\log_{10}$ ρ is 0.21–0.53. The 3-D model differs from the 2-D sections in two ways. First, with 5 m cells and layers that thicken with depth, it gives weaker vertical contrasts at depth. On T5 it does not show the increase in resistivity below about 30–35 m that the 2-D section places at the base of L2; the 3-D values there remain 3–4 Ωm down to 50.8 m. Second, it is more conductive than the 2-D model on T6, which shows the largest mean offset (−0.19 in $\log_{10}$ ρ), consistent with the lower reliability of the T6 data (Section 3.3).

4.3 Agreement at line crossings

At the six line crossings, the two 2-D models differ by factors of 1.4–4.1 (median 2.7; Fig. 5). The best agreement is at T6 × T8 (1.4) and T5 × T6 (1.6), both inside the conductive body, and the worst at T4 × T6 (4.1) and T2 × T6 (3.3). The T4 × T6 crossing is where the T6 data using the electrode at x = 135 m could not be fitted in 3-D (Section 3.3). The 3-D model differs from the two 2-D profiles by geometric-mean factors of 1.3–2.5 (median 1.8). It generally lies between them, except near the surface at T2 × T6 and T6 × T8, where it is lower than both. Where the two 2-D profiles disagree most (T3 × T6, T4 × T6, T2 × T6 and T11 × T12), the 3-D profile is closer to the line with more data: T3 (1.1 against 2.6 for T6), T4 (1.4 against 2.5), T2 (2.1 against 2.8) and T11 (1.7 against 2.2). In four of the five crossings with T6 the 3-D profile is closer to the other line, as expected if the T6 data are the least reliable (Section 3.3). Five of the six crossings involve T6, but the only one that does not, T11 × T12, also differs by a factor of 2.6, so the disagreement between 2-D models is not due to T6 alone.

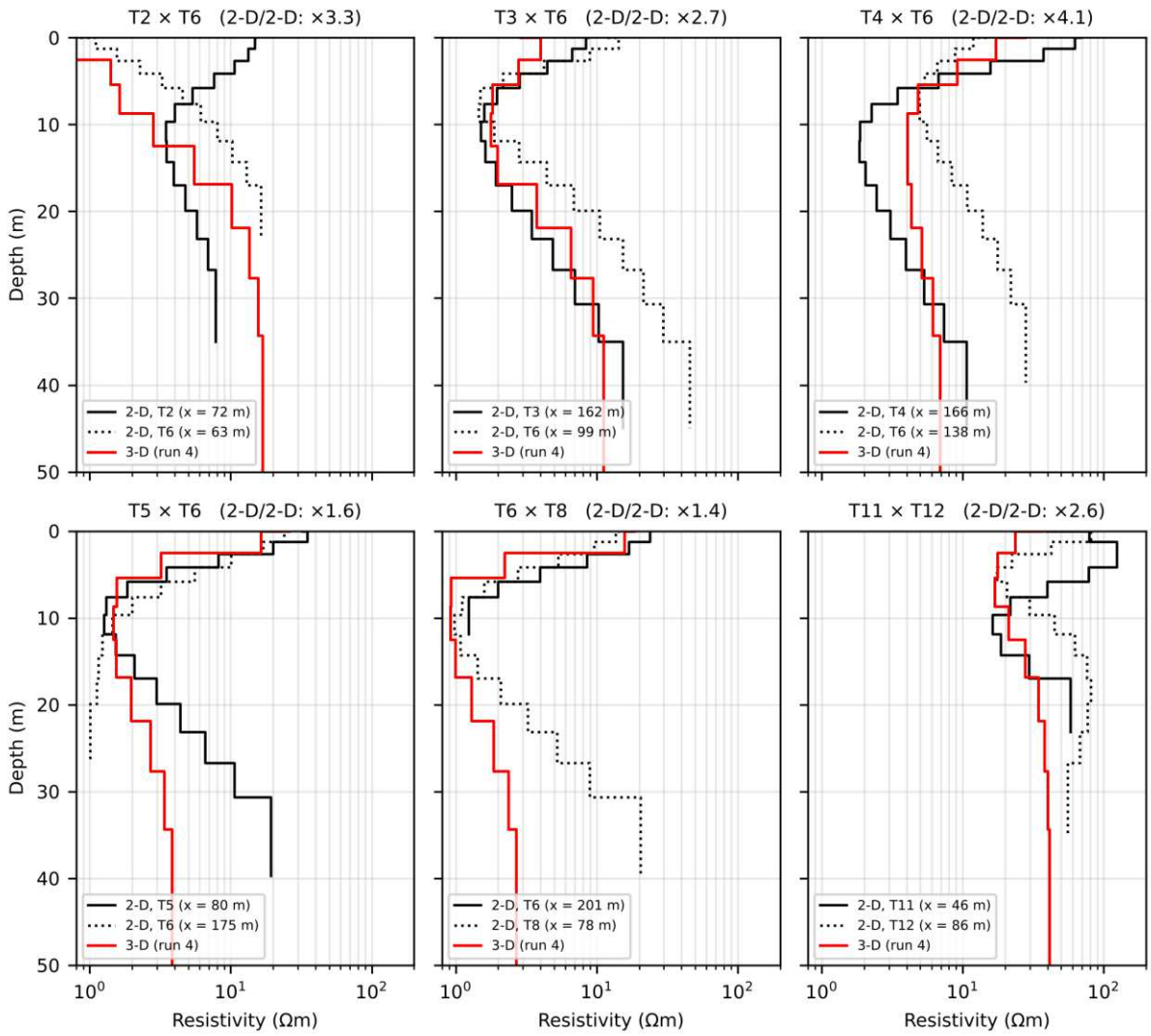


Fig. 5 Resistivity–depth profiles at the six line crossings: 2-D models of the two crossing lines (solid and dotted black) and the 3-D model (red, run 4). The factor in each title is the median difference between the two 2-D profiles

4.4 Stability of the 3-D model

Misfit decreased steadily in all runs, from 28–31% in the first iteration to 5.9–7.1% in the fifth, when the decrease had slowed to 0.7–0.9 percentage points per iteration (Fig. 6a). Runs 3 and 4, which differ only in the 50 removed data, differ by a median of 2.1–2.7% in every layer (Fig. 6b). Removing these data therefore changed the model little, mainly along T6. Runs 1 and 4, which differ in forward solver, electrode treatment and first-layer damping, differ by 19–27% in the top two layers but by 6–10% below 8.7 m. Within the alternatives

tested, the deeper structure is therefore much less sensitive to these choices than the near-surface layers.

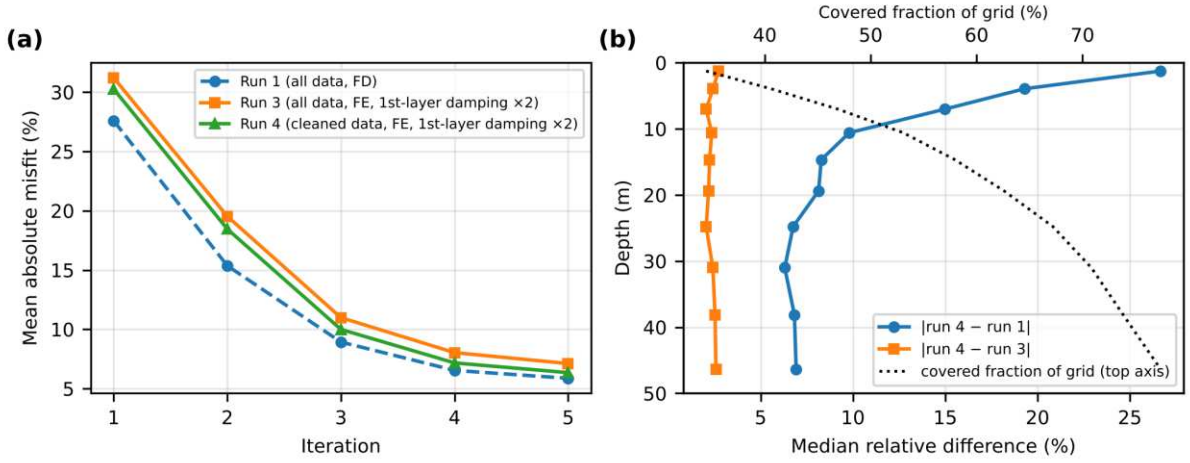


Fig. 6 (a) Mean absolute misfit against iteration for 3-D runs 1, 3 and 4. (b) Median absolute relative difference between the preferred model (run 4) and runs 1 and 3, by layer, over covered cells; dotted line: covered fraction of the grid (top axis)

4.5 Sinkholes and resistivity

The 14 sinkholes inside the grid form two clusters in its north-eastern part (Figs. 1c and 7). The first (five sinkholes, 2010 and 2013) lies along T12 and T9, between their crossing with T11 and the northern end of T1. The second (nine sinkholes, 2010 and 2014) lies between the northern parts of T11 and T1. Averaged over 8.7–21.9 m depth, the 3-D model gives 17–64 Ωm at the sinkhole positions, whereas the median of all covered cells is 9 Ωm and 48% of them exceed 10 Ωm (Fig. 7). None of the sinkholes lies on the conductive body. The nearest cells below 3 Ωm are 57–96 m away at 10.6 m depth and 38–99 m away at 19.4 m depth. Beneath the first cluster the model is about 18–66 Ωm below about 5 m. Beneath the second it is about 40–80 Ωm in the upper 5 m and 12–24 Ωm below about 10 m, although six of these sinkholes are 14–27 m from the nearest electrode, where the model is constrained mainly by the regularisation; the farthest lies within the covered volume only below 16.9 m, and its value is from that layer alone.

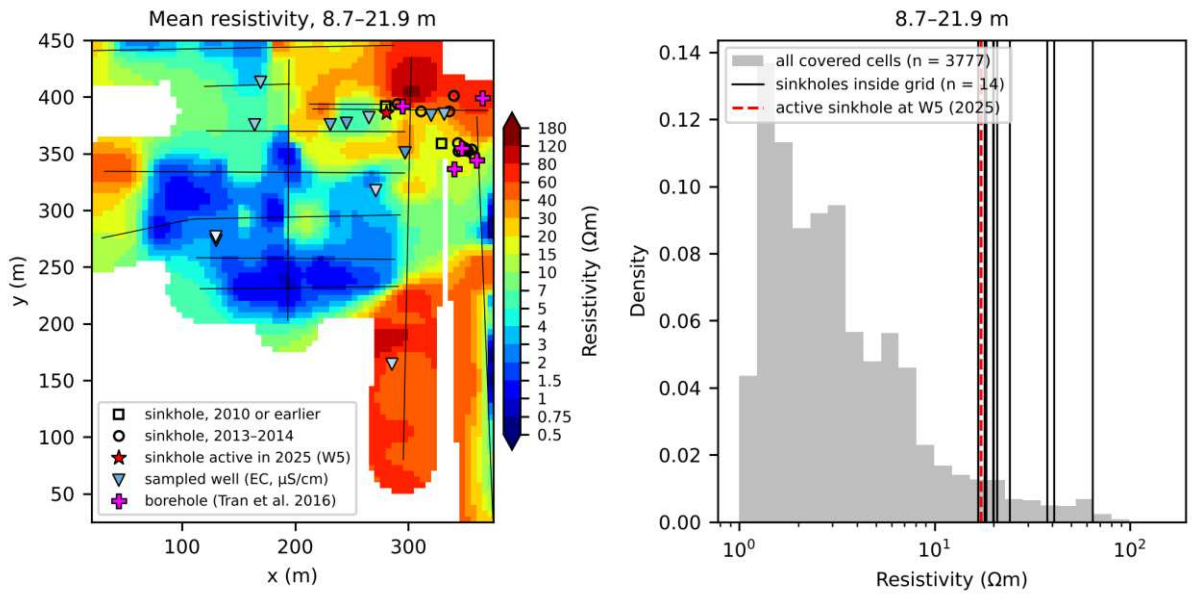


Fig. 7 (a) Geometric-mean resistivity of the preferred 3-D model over 8.7–21.9 m depth, with recorded sinkholes (squares: 2010; circles: 2013–2014), sampled wells (triangles, coloured by EC), boreholes (magenta crosses) and the sinkhole active in 2025 (red star). (b) Distribution of the same quantity over all covered cells (grey) and values at the 14 recorded sinkholes inside the grid (vertical lines) and at the active sinkhole at W5 (red dashed line)

Because the sinkholes form only two spatial clusters, the 14 positions are not independent samples, and the association with higher resistivity cannot be tested as if they were. If each cluster is treated as one observation, the chance that both fall on cells above 10 Ωm by random placement within the covered area is about $0.48^2 \approx 0.23$. The clusters are only about 30–55 m apart in the same resistive area, however, so they may amount to a single observation, for which the corresponding probability is about 0.5. The pattern is therefore suggestive, not statistically established. The inventory covered nearly the whole survey grid, so the absence of recorded sinkholes in the west and centre does not reflect a gap in coverage.

The result does not depend on the choice of 3-D run: runs 1–3 give 15–66 Ωm at the same positions. The 2-D sections show the same pattern beside the first cluster (12–56 Ωm on T12 at x = 55–95 m, averaged over the same depth interval) but are more variable beside the second (7–28 Ωm on T1 at x = 30–50 m). Most of the sinkholes occurred 11–12 years before

the survey and were backfilled (Tran et al. 2016), so the ERT images the present state of the ground. Backfill would mainly alter resistivity near the surface, which is one reason for using the 8.7–21.9 m interval in this comparison.

A new sinkhole appeared at the house of well W5 during the survey (Section 3.4). It lies between electrodes 13 and 15 of T12 (x = 60–70 m), about 3 m south of the line, so its position is tied directly to the ERT line. It is 6 m and 13 m from two inventoried sinkholes of 2010 or earlier and 2013, and about 16 m from borehole LK9, which reached carbonate at 9.0 m (Section 4.7); the borehole positions, read from the map of Tran et al. (2016), are less certain (Section 3.5). The new sinkhole may therefore be a renewed collapse near earlier ones. The 2-D section of T12 beside it gives 15–39 Ωm between about 10 and 23 m depth, and the 3-D model about 17 Ωm at 8.7–21.9 m (10–30 Ωm within 10 m); the nearest cells below 3 Ωm are about 54 m away, so it, too, lies off the conductive body.

4.6 Shallow groundwater

All 12 wells hold fresh water: EC_{25} is 343–1654 µS/cm (median 614 µS/cm), TDS 170–795 mg/L, pH 6.1–7.4 and water temperature 22.6–25.8 °C (Table 3). The corresponding ρ_w is 6–30 Ωm. At 2.5–5.4 m, the layer that contains the well bottoms, the 3-D model gives formation factors of 1.8–17 at seven wells, consistent with this water, but 0.3–0.4 at W8 and W11, where the formation is more conductive than the well water. At 8.7–21.9 m the ratio ρ/ρ_w exceeds 1 only at W1, W2, W3 and W12 (1.7–2.6), all on the resistive ground in the east of the grid; W1, W2 and W3 lie close to the sinkhole clusters. At the other eight wells, which overlie the conductive body or its margins, the ratio is 0.10–0.74. W9 and W10 lie about 10 m apart. W9, the deepest well (5 m), has the most saline water (field EC 1592 µS/cm), whereas W10 (2.5–3 m deep) has the freshest (337 µS/cm). W9 was sampled with a bucket rather than a pump, so the sampling method may contribute, but the contrast is consistent with salinity increasing with depth.

Table 3 Hand-dug wells sampled in October 2025. EC: field value; EC_{25}: compensated to 25 °C with a linear coefficient of 0.0187 per °C (Hayashi 2004). $\rho_w = 10^4/EC$ (field value). ρ: preferred 3-D model at the well position (2.5–5.4 m: layer containing the well bottoms; 8.7–21.9 m: geometric mean of layers 4–6). –: cell not covered

Well	T (°C)	EC (µS/cm)	EC_{25} (µS/cm)	pH	ρ_w (Ωm)	ρ, 2.5–5.4 m (Ωm)	ρ, 8.7–21.9 m (Ωm)	ρ/ρ_w, 8.7–21.9 m
W1	25.4	722	717	6.6	13.9	35.5	23.1	1.67
W2	25.5	626	620	6.1	16.0	40.6	27.6	1.73
W3	25.8	817	805	6.1	12.2	209.8	32.1	2.62
W4	23.7	475	487	6.9	21.1	–	3.6	0.17
W5	22.6	582	609	6.4	17.2	53.1	7.9	0.46
W6	23.2	748	774	6.5	13.4	43.8	5.1	0.38
W7	23.4	720	742	6.7	13.9	25.4	10.3	0.74
W8	23.0	579	601	6.6	17.3	7.1	5.8	0.34
W9	23.0	1592	1654	6.6	6.3	–	2.7	0.43
W10	24.0	337	343	6.4	29.7	–	2.9	0.10
W11	24.5	603	609	6.8	16.6	5.2	4.1	0.25
W12	25.0	477	477	7.4	21.0	62.3	52.9	2.52

4.7 Comparison with boreholes

Borehole logs and depths in this section are from Tran et al. (2016). LK9 lies 3.4 m from T12 (Fig. 8a). The 2-D section there is 56–92 Ωm in the top 2.6 m (fill to 2.5 m), 12–19 Ωm at 4.1–9.6 m (27 Ωm at 2.6–4.1 m), where the log shows dark-grey sandy clay (2.5–6.3 m) and yellow-brown clay (6.3–9.0 m), and 27–30 Ωm at 9.6–11.9 m and 43–78 Ωm at 11.9–19.9 m, in carbonate logged from 9.0 m to the bottom of the hole at 20 m. The 3-D model shows the same increase more smoothly (25–27 Ωm above 8.7 m, 38–45 Ωm at 12.5–21.9 m). CP04, drilled into a 2014 sinkhole, lies 1.8 m from T1 (Fig. 8b). There resistivity is 52–106 Ωm in the fill (to 4.0 m) and decreases steadily below 2.6 m, to 19–21 Ωm at 7.6–9.6 m (carbonate from 8.0 m) and 7–14 Ωm at 9.6–17.0 m, where the log shows a cavity filled with fluid clay from 10.4 to 17.0 m. The profile does not mark the logged boundaries, but its lowest values lie in the cavity interval. At CP06 and LK10, 14–20 m from the nearest electrode but within the covered volume, the 3-D model gives 14–21 Ωm at 8.7–21.9 m. All five boreholes lie where the 3-D model exceeds 10 Ωm at 8.7–21.9 m; none lies on the conductive body.

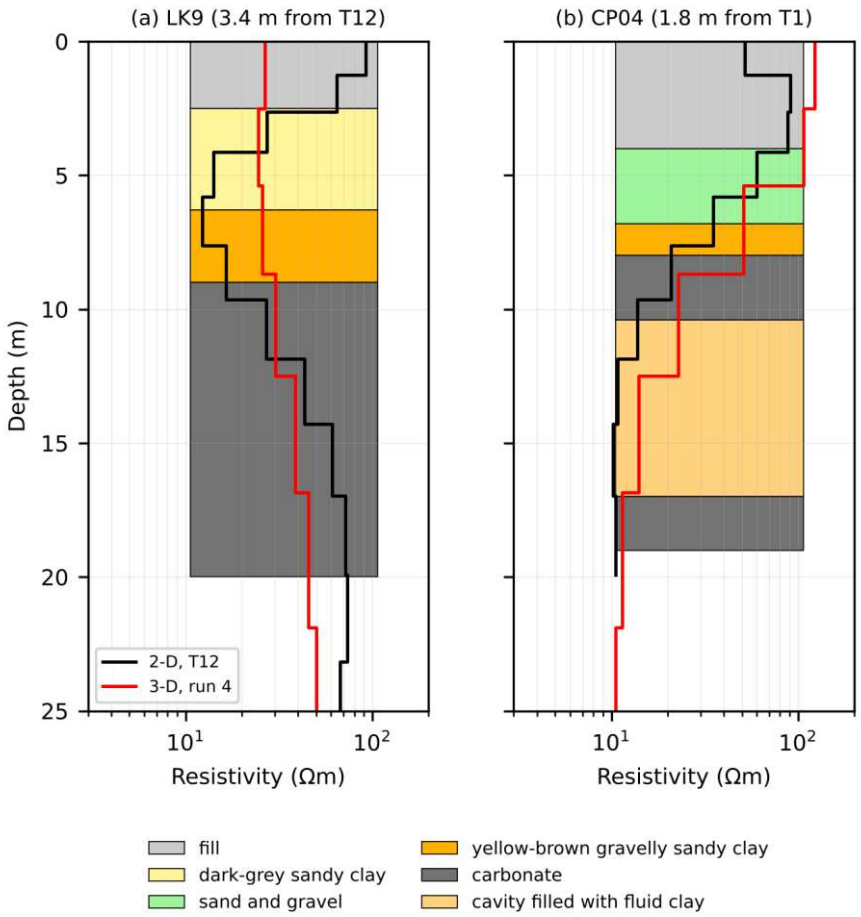


Fig. 8 Logs of boreholes LK9 and CP04, redrawn from Tran et al. (2016), with the resistivity–depth profiles of the nearest 2-D section (black) and of the preferred 3-D model (red) at the borehole

5. Discussion

5.1 How the 2-D and 3-D analyses relate

Each 2-D inversion assumes that resistivity does not vary perpendicular to the line. The disagreement between crossing 2-D models (median factor 2.7, up to 4.1) shows that this assumption fails in this heterogeneous ground: largely, each line images the same ground point differently because each projects off-line structure into its own section. The 3-D inversion removes this inconsistency by requiring one model to explain all data; at the crossings it generally lies between the 2-D models (Section 4.3). The two analyses therefore answer different questions. The 2-D sections have finer vertical resolution beneath each line

and are the better guide to layer boundaries there; for example, T5 places the base of the conductive layer at about 30–35 m, which the smoother 3-D model does not resolve (Figs. 2 and 5), and beside LK9 the 2-D section shows the rise from the clays into the carbonate more clearly than the 3-D model (Fig. 8). The 3-D model is the only one that is consistent at the crossings, and it is the only basis for mapping units between lines and for comparing them with the positions of the sinkholes, most of which do not lie on a line. Between lines it is largely an interpolation imposed by the regularisation: the east–west lines are about 5–45 m apart and the north–south lines 65–105 m apart, far more than the electrode spacing that Papadopoulos et al. (2007) recommend as the maximum line separation. We therefore interpret only features that are seen on several lines and in both analyses, such as the conductive body and the resistive ground in the north-east. The values beneath the second sinkhole cluster, up to 27 m from the nearest electrode, rest mainly on the 3-D model and do not fully meet this criterion.

5.2 What the conductive and resistive units represent

Where drilled, in the north-east, the ground in which the 3-D model exceeds 10 Ωm at 8.7–21.9 m is carbonate under 7.6–9.0 m of cover (Section 4.7). The rock is not uniformly resistive: 43–78 Ωm where intact at LK9, but 7–14 Ωm where a cavity filled with clay was logged at CP04, values that overlap those of the clay cover at LK9 (12–19 Ωm). Both the cover and the rock there are, however, several times more resistive than the conductive body (below 3 Ωm), so the contrast probably reflects less saline pore water as well as lithology.

Beneath the centre and west, the conductive layer reaches median depths of about 20–45 m, locally about 51 m, and on many profiles its base is not reached (Section 4.1; Fig. A2). Values of 1–3 Ωm over tens of metres are comparable with those of shallow coastal sediments holding water of near-seawater salinity, for example about 1 Ωm at 25–30 g/L in the Venice Lagoon (de Franco et al. 2009), and the area lay seaward of the pre-1966 shoreline

(Tran et al. 2016). We therefore infer that the bedrock surface deepens beneath the centre and west and is overlain there by thick saline cover, possibly with clay adding surface conduction (Waxman and Smits 1968). This cover comprises the fill and the sediment below it, which ERT cannot separate; the fill alone is 2.5–4.4 m thick where drilled (Tran et al. 2016). The lithology of the resistive substratum beneath the centre and west is unknown: it may be carbonate or Hon Gai clastic rock.

Beneath the southern part of T11 there is no conductive layer, and resistivity is 35–120 Ωm from the surface to 27–51 m depth. This may be a carbonate high or thick coarse fill. A carbonate surface 18–23 m deep, as shown there on the top-carbonate map of Tran et al. (2016), would require cover of 35–120 Ωm, unlike the conductive cover elsewhere in the grid; a borehole on southern T11 would decide between these possibilities.

The wells show that the shallow groundwater has exchanged with fresher water since reclamation. Water at 2.5–5 m is now fresh in all 12 wells, residents report that several were brackish or saline when dug, and the pair W9–W10 suggests that salinity increases with depth. Beneath most of the grid the formation at 8.7–21.9 m is more conductive than the well water (ρ/ρ_w = 0.10–0.74), which in clean sediment requires pore water at least 1.4–10 times more saline than in the wells: the fresh water forms a thin cap over saline water. The four wells with ρ/ρ_w above 1 stand on more resistive ground, where the interval may be largely rock, so their ratio says little about salinity at that depth. The freshening of the shallow water is seen across the grid and therefore does not distinguish the sinkhole area.

5.3 Sinkholes, cover thickness and groundwater movement

All 14 recorded sinkholes and the sinkhole active in 2025 lie off the conductive body, in the north-east of the grid, where carbonate lies at 7.6–9.0 m depth (Sections 4.5 and 4.7). The control that the ERT and the boreholes show is therefore structural: the sinkholes occur where

thin cover rests on carbonate, and none is recorded where thick saline cover fills the deeper bedrock surface. Sinkholes in covered ground need openings into which material can move, erodible material and moving water (Gutiérrez et al. 2014). Openings are documented beneath two of the three drilled sinkholes (cavities filled with fluid clay at CP04 and LK10), although CP06 found none to 12.5 m (Tran et al. 2016), so karst is a possible contributor.

Groundwater movement is the process we propose to link this structure to the sinkholes, but a single ERT survey images a static state and does not measure flow. Where thin cover rests on carbonate rock, locally with clay-filled cavities, near the stream, fluctuations of the water table driven by rainfall, tides and changes in stream level could move water, fresh or saline, between cover and rock; beneath tens of metres of saline cover such exchange is likely to be weaker. Laboratory and numerical studies show that cyclic flow erodes soil faster than steady flow, and that the hydraulic gradient controls how fast cavities grow (Mukunoki et al. 2012; Karoui et al. 2018; Zhang et al. 2020). Suffosion within the fill towards drains or the stream bank is an alternative or additional path (Tufano et al. 2022); our data cannot show whether a given sinkhole began in the fill or at the rock contact.

The strongest part of the argument is the observation itself: the absence of sinkholes on the conductive body holds in all four 3-D runs (15–66 Ωm at the sinkholes) and in the 2-D section beside the first cluster. Its weak parts are that the two clusters lie only 30–55 m apart and amount to about one observation (Section 4.5), that the conductive body has not been drilled, and that shallow rock and proximity to the stream coincide in the north-east, so their effects cannot be separated. The resistive ground beneath southern T11 provides a partial check: no sinkhole is recorded there. If that ground is also shallow carbonate, thin cover over rock is not sufficient on its own, and a further condition, such as erodible clay at the rock contact or stronger groundwater exchange near the stream, is required; if it is coarse fill, the check does not apply. The groundwater hypothesis can be tested directly: repeated ERT over

tidal and seasonal cycles should show resistivity changes in the north-east but little change in the conductive body, as time-lapse ERT has resolved seasonal changes in saltwater intrusion elsewhere (de Franco et al. 2009), and water levels in wells and piezometers near the stream should follow the tide more closely over the shallow carbonate than over the thick cover.

6. Conclusions

(1) Crossing 2-D models differ by a median factor of 2.7, largely because the ground is three-dimensional and, on T6, partly because of lower data quality. A joint 3-D model is consistent by construction and departs from them by a median factor of 1.8; it is the only consistent basis for mapping units between lines, whereas the 2-D sections are the better guide to layer boundaries beneath each line. (2) The 3-D model maps a conductive body (mostly below 3 Ωm) beneath the centre and west of the grid, where the 2-D sections place its base at about 20–50 m or below the model, and more resistive ground in the north-east and beneath southern T11; below 8.7 m it changes by 6–10% between the inversion settings tested. (3) Three boreholes in the north-east reached carbonate at 7.6–9.0 m; beside one, resistivity rises into intact carbonate, and beside another it is lowest where a clay-filled cavity was logged. (4) All 14 recorded sinkholes lie on 15–66 Ωm ground in every 3-D run, and neither they nor a sinkhole active in 2025 lie on the conductive body. (5) We interpret the conductive body as thick saline cover over a deepening bedrock surface and the north-eastern ground as carbonate under thin cover: the sinkholes occur where the cover is thin over carbonate rock that locally contains clay-filled cavities. Suffosion of the cover into karst driven by groundwater movement is consistent with this but has not been measured. Beneath southern T11, resistive ground extends from the surface to at least 27–51 m; whether it is a carbonate high or coarse fill remains to be tested by drilling. The association rests on one sinkhole-bearing area and should be tested by time-lapse ERT and water-level monitoring.

Acknowledgements

This research was funded by the Department of Science and Technology of Quang Ninh City under grant number NV.CT.H49.2025.08 and by the Vietnam Academy of Science and Technology (VAST) under grant number CN40000.01/26-28. The authors acknowledge the use of Claude (Anthropic) as an AI writing assistant during the preparation of this manuscript for language editing, manuscript checking and assistance with data-processing and plotting scripts; all results were verified by the authors.

Declarations

Competing interests

The authors have no relevant financial or non-financial interests to disclose.

Data availability

The data that support the findings of this study are available from the corresponding author on reasonable request.

Author contributions

Conceptualization and field investigation: Nguyen Nhu Trung and Nguyen Van Duong. Data acquisition and processing: Nguyen Nhu Trung, Bui Van Nam, Tran Van Kha, Pham The Truyen, Ha Thi Giang, Nguyen Van Diep. Formal analysis and interpretation: Nguyen Nhu Trung and Nguyen Van Duong. Writing – original draft: Nguyen Nhu Trung. Writing – review and editing: all authors. Funding acquisition: Nguyen Van Duong and Pham The Truyen. All authors read and approved the final manuscript.

References

Archie GE (1942) The electrical resistivity log as an aid in determining some reservoir characteristics. Trans AIME 146:54–62. https://doi.org/10.2118/942054-G

Carbonel D, Rodríguez-Tribaldos V, Gutiérrez F, Galve JP, Guerrero J, Zarroca M, Roqué C, Linares R, McCalpin JP, Acosta E (2015) Investigating a damaging buried sinkhole cluster in an urban area (Zaragoza city, NE Spain) integrating multiple techniques: geomorphological surveys, DInSAR, DEMs, GPR, ERT, and trenching. Geomorphology 229:3–16. https://doi.org/10.1016/j.geomorph.2014.02.007

Carrazza LP, Moreira CA, Helene LPI (2016) Gully cavity identification through electrical resistivity tomography. Rev Bras Geofís 34(2):241–250. https://doi.org/10.22564/rbgf.v34i2.799

Chambers JE, Ogilvy RD, Kuras O, Cripps JC, Meldrum PI (2002) 3D electrical imaging of known targets at a controlled environmental test site. Environ Geol 41(6):690–704. https://doi.org/10.1007/s00254-001-0452-4

Chambers JE, Kuras O, Meldrum PI, Ogilvy RD, Hollands J (2006) Electrical resistivity tomography applied to geologic, hydrogeologic, and engineering investigations at a former waste-disposal site. Geophysics 71(6):B231–B239. https://doi.org/10.1190/1.2360184

Cong-Thi D, Dieu LP, Thibaut R, Paepen M, Ho HH, Nguyen F, Hermans T (2021) Imaging the structure and the saltwater intrusion extent of the Luy River coastal aquifer (Binh Thuan, Vietnam) using electrical resistivity tomography. Water 13(13):1743. https://doi.org/10.3390/w13131743

Dang VK, Nguyen TD, Dao NH, Duong TL, Dinh XV, Weber C (2021) Land subsidence induced by underground coal mining at Quang Ninh, Vietnam: persistent scatterer

525 interferometric synthetic aperture radar observation using Sentinel-1 data. Int J Remote
526 Sens 42(9):3563–3582. https://doi.org/10.1080/01431161.2021.1875513

527 de Franco R, Biella G, Tosi L, Teatini P, Lozej A, Chiozzotto B, Giada M, Rizzetto F, Claude
528 C, Mayer A, Bassan V, Gasparetto-Stori G (2009) Monitoring the saltwater intrusion by
529 time lapse electrical resistivity tomography: the Chioggia test site (Venice Lagoon, Italy).
530 J Appl Geophys 69:117–130. https://doi.org/10.1016/j.jappgeo.2009.08.004

531 Deceuster J, Etienne A, Robert T, Nguyen F, Kaufmann O (2014) A modified DOI-based
532 method to statistically estimate the depth of investigation of dc resistivity surveys. J Appl
533 Geophys 103:172–185. https://doi.org/10.1016/j.jappgeo.2014.01.018

534 Gutiérrez F, Parise M, De Waele J, Jourde H (2014) A review on natural and human-induced
535 geohazards and impacts in karst. Earth-Sci Rev 138:61–88.
536 https://doi.org/10.1016/j.earscirev.2014.08.002

537 Hayashi M (2004) Temperature-electrical conductivity relation of water for environmental
538 monitoring and geophysical data inversion. Environ Monit Assess 96:119–128.
539 https://doi.org/10.1023/B:EMAS.0000031719.83065.68

540 Karoui T, Jeong S-Y, Jeong Y-H, Kim D-S (2018) Experimental study of ground subsidence
541 mechanism caused by sewer pipe cracks. Appl Sci 8(5):679.
542 https://doi.org/10.3390/app8050679

543 Loke MH, Barker RD (1996) Rapid least-squares inversion of apparent resistivity
544 pseudosections by a quasi-Newton method. Geophys Prospect 44(1):131–152.
545 https://doi.org/10.1111/j.1365-2478.1996.tb00142.x

546 Loke MH, Acworth I, Dahlin T (2003) A comparison of smooth and blocky inversion
547 methods in 2D electrical imaging surveys. Explor Geophys 34(3):182–187.
548 https://doi.org/10.1071/EG03182

549 Loke MH, Chambers JE, Rucker DF, Kuras O, Wilkinson PB (2013) Recent developments in
550 the direct-current geoelectrical imaging method. J Appl Geophys 95:135–156.
551 https://doi.org/10.1016/j.jappgeo.2013.02.017

552 Mesri G, Funk JR (2015) Settlement of the Kansai International Airport Islands. J Geotech
553 Geoenviron Eng 141(2):04014102. https://doi.org/10.1061/(ASCE)GT.1943-
554 5606.0001224

555 Mukunoki T, Kumano N, Otani J (2012) Image analysis of soil failure on defective
556 underground pipe due to cyclic water supply and drainage using X-ray CT. Front Struct
557 Civ Eng 6(2):85–100. https://doi.org/10.1007/s11709-012-0159-5

558 Nguyen F, Kemna A, Antonsson A, Engesgaard P, Kuras O, Ogilvy R, Gisbert J, Jorreto S,
559 Pulido-Bosch A (2009) Characterization of seawater intrusion using 2D electrical
560 imaging. Near Surf Geophys 7(5–6):377–390. https://doi.org/10.3997/1873-
561 0604.2009025

562 Nguyen GC, Dang KV, Vu TA, Nguyen AK, Weber C (2022) Ha Long—Cam Pha cities
563 evolution analysis utilizing remote sensing data. Remote Sens 14(5):1241.
564 https://doi.org/10.3390/rs14051241

565 Nguyen NT, Dang XP, Trinh HT, Bui VN, Nguyen VD (2025a) Mapping freshwater and
566 seawater intrusion using electrical resistivity tomography and physicochemical data: an
567 application in Coto Island, Gulf of Tonkin. Marine Geophysical Research (2025) 46:1
568 https://doi.org/10.1007/s11001-025-09562-x

569 Nguyen NT, Dang XP, Trinh HT, Bui VN, Nguyen VD (2025b) Assessment of seasonal
570 groundwater variability using Time-Lapse electrical resistivity tomography in the Co to
571 Island area, Gulf of Tonkin, Vietnam. Marine Geophysical Research (2026) 47:1.
572 https://doi.org/10.1007/s11001-025-09599-y

573 Oldenburg DW, Li Y (1999) Estimating depth of investigation in dc resistivity and IP
574 surveys. Geophysics 64(2):403–416. https://doi.org/10.1190/1.1444545
575 Papadopoulos NG, Tsourlos P, Tsokas GN, Sarris A (2007) Efficient ERT measuring and
576 inversion strategies for 3D imaging of buried antiquities. Near Surf Geophys 5(6):349–
577 361. https://doi.org/10.3997/1873-0604.2007017
578 Seequent (2022) RES3DINVx64 ver. 3.19: rapid 3-D resistivity & IP inversion using the
579 least-squares method. User manual, October 2022.
580 https://help.seequent.com/ResXDinv/en-
581 GB/Content/Resources/DownloadableAssets/Res3dinvx64.pdf
582 Seequent (2025) RES2DINV ver. 2025.1: rapid 2D resistivity & IP inversion. User manual,
583 March 2025. https://help.seequent.com/ResXDinv/en-
584 GB/Content/Resources/DownloadableAssets/Res2DInv_Manual.pdf
585 Sevil J, Gutiérrez F, Zarroca M, Desir G, Carbonel D, Guerrero J, Linares R, Roqué C,
586 Fabregat I (2017) Sinkhole investigation in an urban area by trenching in combination
587 with GPR, ERT and high-precision leveling. Mantled evaporite karst of Zaragoza city,
588 NE Spain. Eng Geol 231:9–20. https://doi.org/10.1016/j.enggeo.2017.10.009
589 Tran QC et al (2016) Nghiên cứu xác định nguyên nhân và đề xuất giải pháp giảm thiểu sụt
590 lún đất trên địa bàn thành phố Cẩm Phả [Determining the causes of land subsidence in
591 Cam Pha city and proposing mitigation measures]. Final report of the state-level project
592 105/ĐXPS.01/2014, funded by the National Foundation for Science and Technology
593 Development (NAFOSTED). Institute of Geology, Vietnam Academy of Science and
594 Technology, Hanoi (in Vietnamese)

595 Tufano R, Guerriero L, Annibali Corona M, Bausilio G, Di Martire D, Nisio S, Calcaterra D
596 (2022) Anthropogenic sinkholes of the city of Naples, Italy: an update. Nat Hazards
597 112(3):2577–2608. https://doi.org/10.1007/s11069-022-05279-x

598 Waxman MH, Smits LJM (1968) Electrical conductivities in oil-bearing shaly sands. Soc Pet
599 Eng J 8:107–122. https://doi.org/10.2118/1863-A

600 Zhang DM, Du WW, Peng MZ, Feng SJ, Li ZL (2020) Experimental and numerical study of
601 internal erosion around submerged defective pipe. Tunn Undergr Space Technol
602 97:103256. https://doi.org/10.1016/j.tust.2019.103256

603 Zhou W, Beck BF, Adams AL (2002) Effective electrode array in mapping karst hazards in
604 electrical resistivity tomography. Environ Geol 42(8):922–928.
605 https://doi.org/10.1007/s00254-002-0594-z

606

Appendix

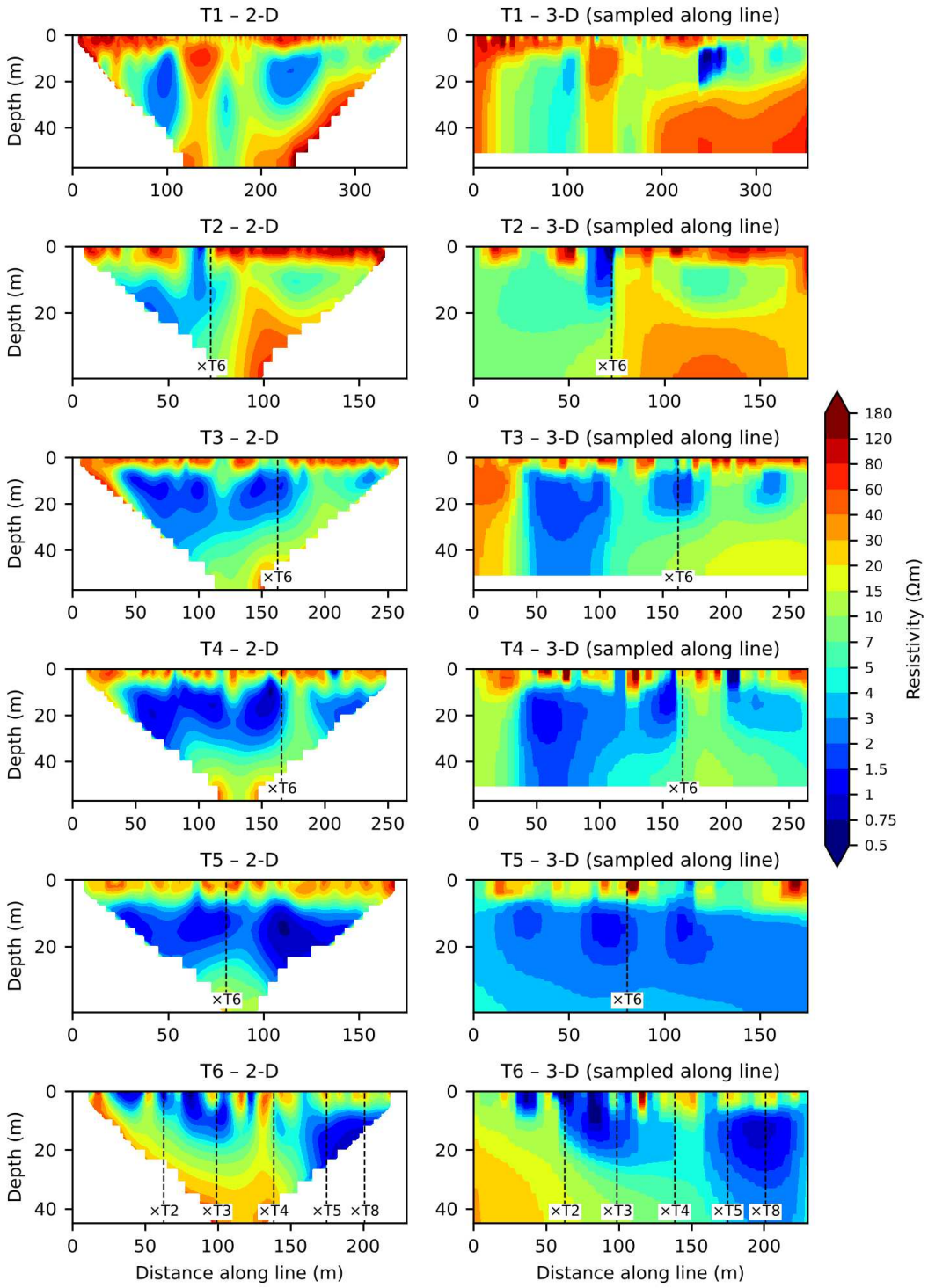


Fig. A1 2-D (left) and 3-D (right) sections for all twelve lines: (a) T1–T6; (b, next page) T7–T12, with the same colour scale as Fig. 2. The 3-D model extends to 50.8 m; the 2-D sections of T1, T3 and T4 are shown to their full depth (57 m) so that the base of the conductive layer is visible where it lies below the 3-D model

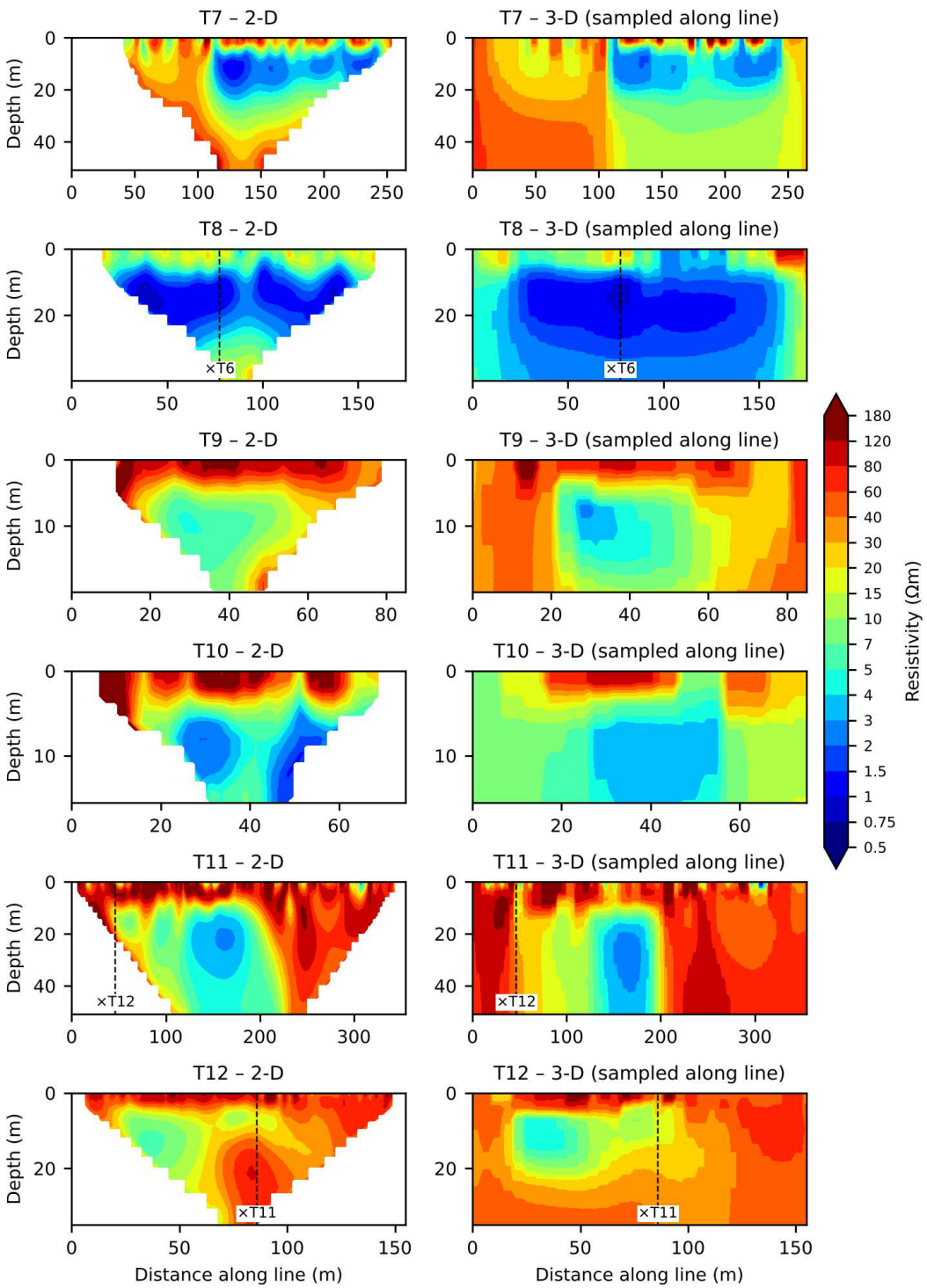
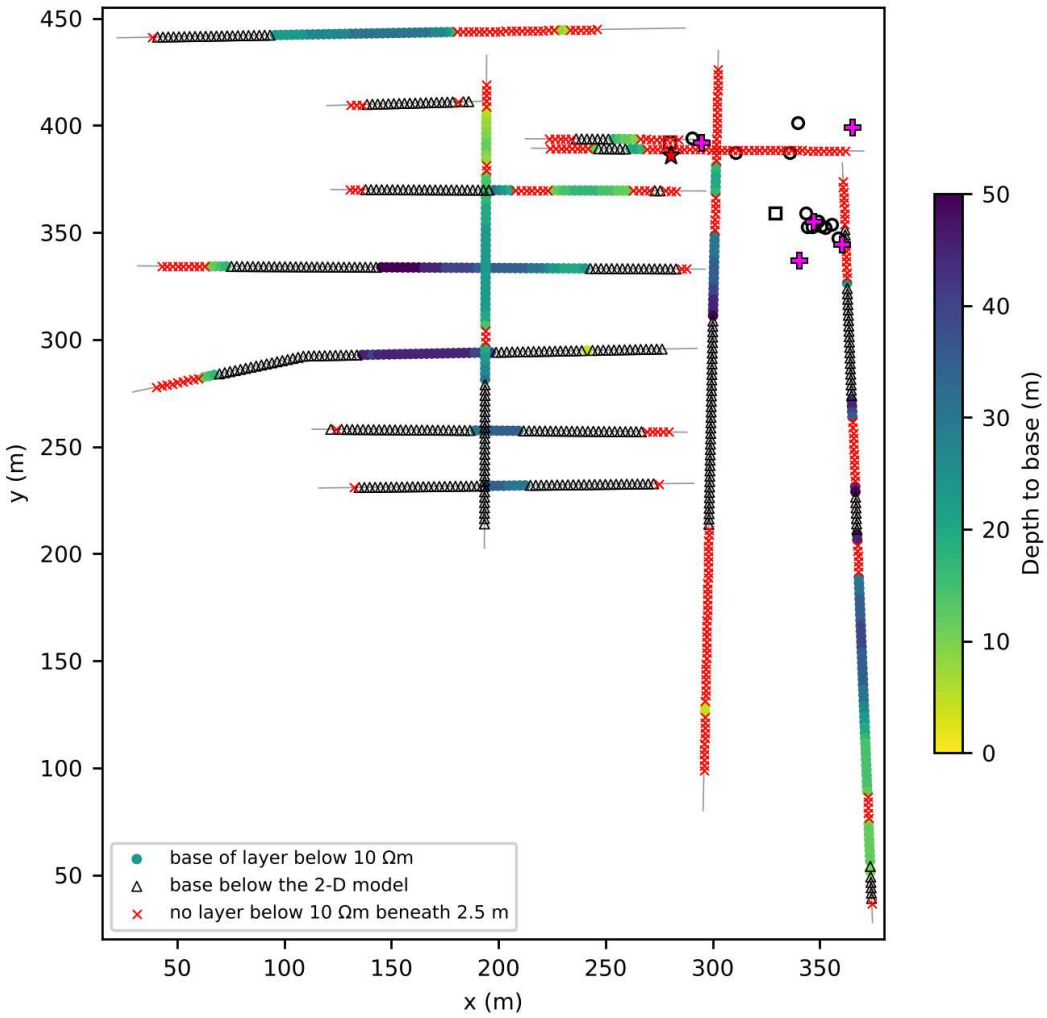


Fig. A1 (continued) (b) Lines T7–T12



615
616 **Fig. A2** Depth to the base of the conductive layer L2 along the 2-D sections, taken as the depth at
617 which resistivity rises back above 10 Ωm beneath the shallowest cell below 10 Ωm (ignoring the top
618 2.5 m). Triangles: L2 continues to the base of the 2-D model; crosses: no cell below 10 Ωm beneath
619 2.5 m. Open symbols: recorded sinkholes; magenta crosses: boreholes; star: sinkhole active in 2025

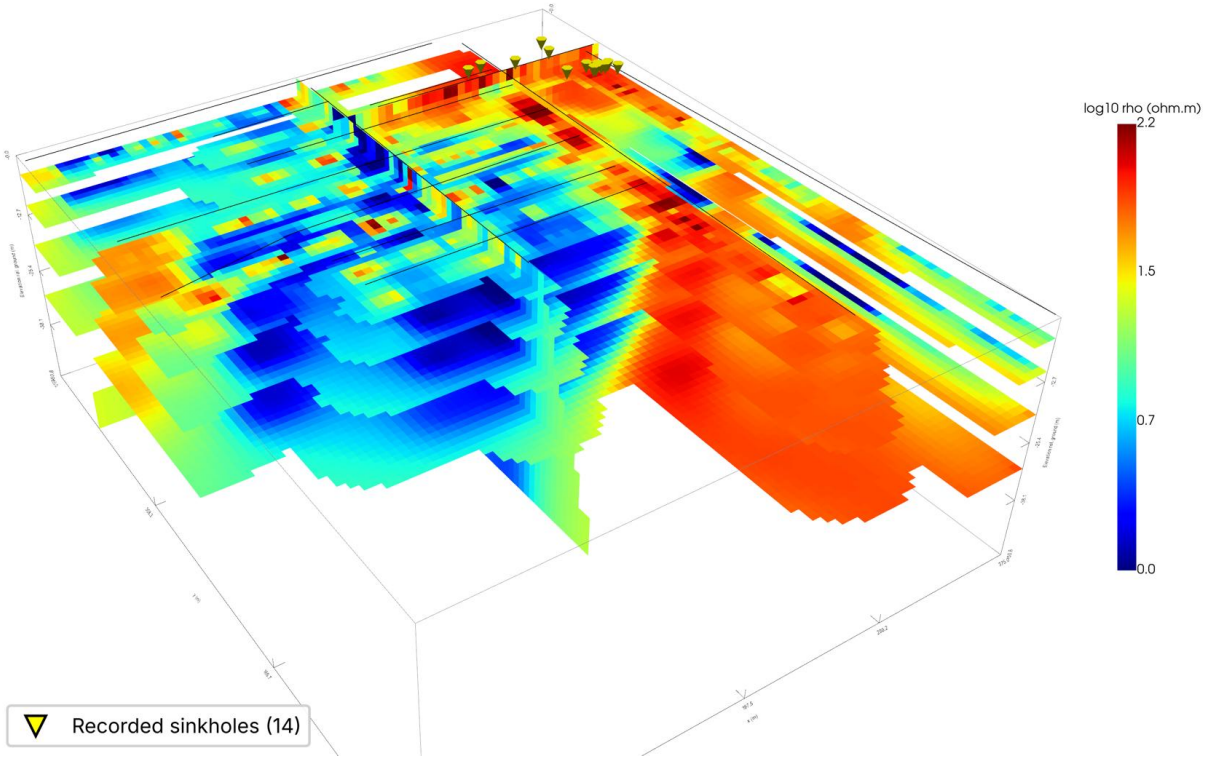


Fig. A3 Perspective view of the preferred 3-D model (run 4): horizontal slices at 4.0, 10.6, 19.4 and 31.0 m depth and vertical slices along T6 and T12, restricted to covered cells. Colour scale: $\log_{10}$ resistivity (0 = 1 Ωm, 1 = 10 Ωm, 2 = 100 Ωm); vertical exaggeration ×3. Yellow cones: recorded sinkholes